Analyses of Oxygen Precipitates in CZ-Si by X-ray Diffuse Scattering Using Parallel X-ray Beam

Tomoyuki Horikawa[1,4], Yoshiyuki Tsusaka[2], Junji Matsui[2,3], Tetsuya Tohei[4], Yusuke Hayashi[4, 5], and Akira Sakai[4]

[1] *GlobalWafers Japan Co., Ltd., 6-861-5, Seiro-machi Higashiko, Kitakanbara-gun, Niigata 957-0101, Japan.*

[2] *Graduate School of Science, University of Hyogo, 3-1-2, Kouto, Kamigori-cho, Ako-gun, Hyogo 678-1205, Japan.*

[3] *Hyogo Science and Technology Association, Synchrotron Radiation Center, 1-490-2, Kouto, Shingu-cho, Tatsuno, Hyogo 679-5165, Japan.*

[4] *Graduate School of Engineering Science, Osaka University, 1-3 Machikaneyama-cho, Toyonaka, Osaka 560-8531, Japan.*

[5] *National Institute for Materials Science, 1-2-1 Sengen, Tsukuba, Ibaraki 305-0047, JAPAN*

E-mail: Tomoyuki_Horikawa@sas-globalwafers.co.jp

Abstract

X-ray diffuse scattering (XDS) is a powerful technique for studying the formation of bulk defects that cause lattice distortions in Czochralski silicon (CZ-Si). To quantitatively analyze oxygen precipitates (OP) in CZ-Si that are below the detection limit of infrared tomography (IR-T), we investigated the relationship between the XDS intensity and the IR-T analysis results obtained from various samples. X-ray rocking curve (XRC) profiles, which included XDS near 400 diffraction peaks on the obliquely polished surface of the CZ-Si wafers, were obtained using a synchrotron radiation X-ray diffractometer. By deriving the XDS-integrated intensities from these XRC profiles, we identified a significant and quantitative relation between the XDS characteristic intensity and the volume density and size of the OPs measured by IR-T. We also find that X-rays scattered from depths below 40 μm contribute to the characteristic intensity of XDS. These results provide critical information for quantitative analysis of OPs using XDS.

1. Introduction

Recently, as the design scale of semiconductor devices has decreased, device structures have become more complicated. Examples include stacked structures in three-dimensional NAND flash memory[1)] and stacking of CMOS and memory devices found in image sensors.[2-3)] The Czochralski growth method is primarily used to grow single-crystal Si crystals, which incorporate oxygen impurities caused by the solid dissolution of oxygen from the crucibles used for crystal growth.[4)] Oxygen precipitates (OPs) in Czochralski silicon (CZ-Si) wafers contribute to the gettering of heavy metal impurities in devices and improve the mechanical strength of Si wafers.[5)] However, the OPs remaining in the device region can cause failures owing to current leakage.[6-7)] Therefore, control of OPs near the device formation region in the CZ-Si wafer (i.e., the extreme surface layer of the CZ-Si wafer) is essential for developing advanced devices.[8-10)]

Infrared tomography (IR-T) is universally used to detect OPs with sizes of ≥20 nm and densities of $\geq 10^6$ cm^{-3}.[11)] Conversely, compared with conventional methods, such as IR-T, transmission electron microscopy (TEM), and defect etching, synchrotron parallel-beam X-ray rocking curve (XRC) analysis is a highly sensitive method for detecting OPs. X-ray diffuse scattering (XDS) analysis near the Bragg diffraction is a powerful technique for studying point defects or defect clusters that cause lattice distortion in single-crystal materials. Trinkaus[12)] and Dederichs[13)] systematically analyzed the intensity and morphology of Huang scattering from the long-range elastic strain field surrounding the defect. In addition, Sama et al.[14)], Bublik et al.[15)], and Caha and Meduna[16)] attempted to qualitatively and quantitatively analyze the formation of OPs in CZ-Si crystals based on the XDS intensity profiles attributed to OPs of ≥100 nm. In this study, to precisely control the OPs for the development of advanced CZ-Si, we developed a method to quantify the volume density and size of OPs based on the XDS intensity resulting from the distortion caused by small-sized OPs in the CZ-Si. We also investigated the contribution of the X-ray penetration depth to the XDS intensity of the OPs.

2. Theory of X-ray diffuse scattering[17-19)]

The XDS intensity of the defect clusters such as OPs is generally very weak. Therefore, the scattering cross sections of XDS are described based on the kinematical theory of diffraction, which does not consider multiple scattering. The scattering cross sections of XDS from randomly distributed defects are given by[18)]

$$\frac{d\sigma(\mathbf{K})}{d\Omega} = |r_e f(\mathbf{K})|^2 |A(\mathbf{K})|^2, \qquad (1)$$

where r_e is the classical electron radius and $f(\mathbf{K})$ is the atomic scattering factor, including the thermal and polarization effects. $\mathbf{K}$ is the scattering vector given by $\mathbf{K} = \mathbf{h} + \mathbf{q}$, where $\mathbf{h}$ is a reciprocal lattice vector and $\mathbf{q}$ is a vector in the Brillouin zone. $A(\mathbf{K})$ is the diffuse scattering amplitude for randomly distributed defects, which in the single-defect approximation is given by

$$A(\mathbf{K}) = \sum_j e^{i\mathbf{K}\cdot\mathbf{r}_j^L} + \sum_i e^{i\mathbf{q}\cdot\mathbf{r}_i}\left(e^{i\mathbf{K}\cdot\mathbf{s}_i} - 1\right), \qquad (2)$$

where $\mathbf{r}_j^L$ is the position of the atoms in the defect clusters and $\mathbf{s}_i$ is the displacement from the *i*-th periodic lattice site. The first term represents direct Laue scattering from the core of the OPs. The scattering in this region corresponds to the asymptotic or Stokes-Wilson scattering region ($q > 1/R$, where R is the defect radius), and the average scattering intensity decreases with q^{-4}. Thus, the slope of the curve of $\log I = f(\log q)$ in this scattering region is -4, where I is scattering intensity. The second term represents the scattering from the surrounding atoms $\mathbf{s}_i$ displaced from their regular lattice positions by the strain field surrounding the OPs. The scattering in this region corresponds to the Huang scattering region ($q \ll 1/R$), and the average scattering intensity decreases with q^{-2}. When the defect concentration is low, scattering due to thermal lattice vibrations dominates over XDS owing to lattice distortion, and experimentally obtaining information regarding the Huang scattering region becomes challenging. Therefore, in this study, we obtained the difference between the XRC profiles of CZ-Si and Si samples with few defects to eliminate the effect of thermal diffuse scattering.

The XDS measured with symmetric Bragg geometry was quantitatively correlated with the scattering cross section from the distribution of OPs through:[19)]

$$I(\mathbf{K}) = \frac{I_0}{2\mu_0} \sum_j c_j\left(R_j\right) \frac{d\sigma_j\left(\mathbf{K},R_j\right)}{d\Omega} (\Delta\Omega), \qquad (3)$$

where I_0 is the incident beam power, μ_0 is the linear absorption coefficient, $c_j\left(R_j\right)$ is the volume concentration of defect clusters of radius R_j, $d\sigma_j\left(\mathrm{K}, R_j\right)/d\Omega$ is the differential cross section for defect clusters of radius R_j and $\Delta\Omega$ is the solid angle subtended by the detector. In other words, a quantitative relation exists between the integrated intensity of XDS and the size and volume density of the OPs.

The X-ray penetration depth (l_{abs}) into the crystal in the symmetric Bragg geometry is given by

$$l_{abs} = \frac{\sin\theta_B}{2\mu_0}, \qquad (4)$$

where θ_B is the Bragg angle. The contribution of the X-ray penetration depth to the XDS intensity of the OPs is key information in XDS where the scattering intensity is very weak.

3. Experimental methods

Several boron-doped CZ-Si (100) wafers, with diameters of 300 mm, were cut from a single CZ-Si crystal and prepared as samples for this study. The interstitial oxygen concentration [Oi] of these samples was 1.23–1.27×10^{18} atoms/cm^{-3} and the specific resistance was 9.4–9.8 Ωcm. These CZ-Si wafers were subjected to ultrahigh temperature rapid thermal oxidation (RTO) to form uniform OPs in the radial direction.[20-22] The temperature was 1350 °C and the holding time was 30 s in a pure O_2 atmosphere. We prepared three samples with different amounts of OPs; the heat-treatment conditions of RTO-treated wafers were changed to enhance oxygen precipitation.[23-24] The temperature, holding time, and furnace fill gas for the multistep heat treatments are listed in Table I. Cross-sectional IR-T images of the OPs obtained from these heat-treated samples are also shown at the bottom of this table. These images show that the number of OPs increased with the depth from the surface of the sample, and the longer the heat treatment time, the more the formed OPs. The average sizes of the OPs derived from the IR-T images were 47, 75, and 82 nm for Samples A–C, respectively. To evaluate the distribution of OPs in the depth direction of the CZ-Si samples using XRC, the sample surfaces were obliquely polished at an angle of 2.87 °, as schematically shown in Fig. 1. Notable, any processing damage left on the sample can affect the XRC profile. Therefore, the surface for X-ray irradiation was carefully polished. Undoped FZ-Si(100) wafers with few OPs were prepared as reference samples. Unlike CZ-Si wafers, FZ-Si wafers are manufactured using a crystal growth method that does not require a quartz crucible. Therefore, FZ-Si wafers do not contain dissolved oxygen concentration, resulting in very few OPs, as shown in the IR-T image in Table I. For all samples, the natural oxide film on the sample surface was removed by hydrogen fluoride (HF)-treatment (≤5%) immediately before the XRC measurement.

Generally, high-brightness X-rays are required to accurately evaluate the XDS. Therefore, we used synchrotron highly parallel X-rays with which the diffractometer, constructed at the BL24XU B1-hatch at SPring-8.[25] We used 15-keV X-rays generated from the undulator and set the beam formation optics with a four-quadrant slit (height 50 μm × width 100 μm) and four (333)Si single crystals monochromators. As shown in Fig. 1, X-rays were incident from

the [011] direction at multiple sites on the inclined surface corresponding to 20 μm interval depth positions of the sample, and $2\theta/\omega$ scan analysis was performed near the 400 XRC diffraction peak under the conditions in Table II. The statistical error from the measurements is an average of 0.75% and a maximum of 1.5%. A scintillation counter was employed as the detector, and the aperture of the slit in front of the detector was 1000 μm high × 1000 μm wide. The optical characteristics of the diffractometer were as follows: direct X-ray intensity: 1.3×10^8 cps, beam size: 46 μm (height) × 150 μm (width), diffraction divergence: 1.8×10^{-4} degrees, and energy divergence: 1.34eV. The beam was narrower than the intrinsic diffraction spread of 4.6×10^{-4} deg for 400 diffractions of Si at 15-keV and exhibited a dynamic range of more than 10^6 cps, which fully satisfied the requirements of this experiment.

4. Results and discussion

Figures 2(a)–(c) depict the XRCs around 400 diffraction points for the three types of CZ-Si samples listed in Table I (referred to as Samples A–C, respectively). The vertical axis represents the diffraction intensity normalized by the diffraction peak intensity, and the horizontal axis represents the diffraction angle converted to a reciprocal lattice coordinate (Q_z). Each graph plots XRCs at the depth positions of 0 to 80 μm with 20 μm intervals, and depth positions of 80 μm to 240 μm with 80 μm intervals from the sample surface for CZ-Si and reference FZ-Si samples. The XDS intensity due to OPs were observed at approximately 2×10^{-5} to 2×10^{-3} Å^{-1} in the XRC of each CZ-Si sample. The XDS intensities were higher at deeper positions in each sample and for samples annealed for a longer period (Samples B and C). These results corresponded well with the distribution of the OPs observed in the IR-T images (Table I). This indicates a strong dependence of the XDS intensity on the OPs.

To evaluate the OPs quantitatively, we derived an integrated intensity from each XDS profile. To exclude the beam spread of the diffractometer (1.8×10^{-4} degree) and the intrinsic diffraction spread of Si (4.6×10^{-4} degree) in the vicinity of the 400 diffraction peak, the integration region was set from 1.2×10^{-5} (3.0×10^{-4} degree) to 3.2×10^{-3} Å^{-1} (8.0×10^{-2} degree). The endpoint was defined as the convergence point of the XDS intensity. Next, the thermal diffuse scattering intensity of Si was subtracted from XDS intensity. This issue was resolved by differentiating the XDS intensity of each sample from that of FZ-Si. Thus, in this study, the integrated intensity of the XDS components attributable to the OPs was defined as the characteristic intensity. The statistical error across the region of characteristic intensity was about 0.5%, and the effect on the detection limit was sufficiently suppressed.

Another issue for the present analysis is the penetration depth of the X-rays, where the OPs information contributes to the characteristic intensity of the XDS. As mentioned above, XDS, a scattering phenomenon at the tail of the diffraction peak, is based on the kinematical theory of diffraction, and the attenuation penetration depth of X-rays into the sample is defined by Eq. (4). The penetration depth of X-rays in this experimental system (15 keV, 400 diffraction) and the samples (Si) was estimated to be approximately 63 μm.

Considering the above issues, we first evaluated the depth of X-ray penetration, which influences the relation between the XDS characteristic intensity and volume density of OPs (VDOP). Figure 3(a) shows the resultant plots for the XDS characteristic intensity and VDOP measured from a depth range of 10–60 μm in Sample A. As schematically shown in Fig. 3(b), the cross-sectional IR-T images were used to measure VDOP in the 1000 μm wide area within a depth range of 10 μm as a unit. Linear relations were clearly observed for all depth ranges and VDOP ranges of 1×10^8 to 5×10^9 cm^{-3}. Conversely, in the region with VDOP $<1 \times 10^8$ cm^{-3}, no relation was observed in the depth range of over 50 μm as the Fig. 3. This result indicated that X-rays scattered from depths below 40 μm contribute to the XDS characteristic intensity with consistency: the value is shallower than the X-ray penetration depth derived from kinematical theory of diffraction. This is possibly because XDS is a low-intensity phenomenon, $<10^{-2}$ relative to the diffraction peak intensity. These results provide key information for the quantitative analysis of OPs below the detection limit of IR-T using XDS. In $2\theta/\omega$ scan, the detection limit may be improved by using high-counting rate detectors such as an avalanche photodiode (APD) detector in the high detection count region and by increasing the accumulation time in the low detection count region.

Figure 4(a) shows the relation between the XDS characteristic intensity and VDOP in areas where OPs were detected by IR-T, when VDOP was estimated from a 40-μm-depth-range × 1000-μm-width area in the cross-sectional IR-T images of Samples A–C, considering the aforementioned X-ray penetration length of 40 μm. The VDOP was found to exhibit a linear relation with the XDS characteristic intensity in the range of 3×10^7 to 5×10^9 cm^{-3} for all samples. However, for a volume density of $\geq 5 \times 10^9$ cm^{-3}, because the overlapping of scattering from OPs makes the counting of the number of defects in the cross-sectional image challenging, quantifying the VDOP value is not easy. Therefore, the approximate curve in the graph ($y = a \cdot x^b$) was drawn at data points below the volume density of 5×10^9 cm^{-3}. The values of the coefficients of the approximate curves ($y = a \cdot x^b$) shown in Fig. 4 are listed in Table III. Similarly, the average volume of OPs (AVOP) was the average value of the volume of individual OPs derived from the scattering intensity

of the OPsin the IR-T within a 40-μm-depth- range × 1000-μm-width area, assuming a spherical shape of OPs. As shown in Fig. 4(b), a relation with the XDS characteristic intensity was clearly observed. We believe that the reason why the plots of Samples B and C do not lie on the extrapolation curve of Sample A is that the volume of OPs was underestimated due to the upper limit of the scattering intensity, which includes the discriminability of individual OPs in IR-T due to the high density of the OPs. The XDS characteristic intensities of Samples B and C, with OPs with the average size of >70 nm, and Sample A, with those of <50 nm, were different by one order of magnitude; however, good relations were observed for both VDOP and AVOP. This is consistent with the fact that the XDS intensity in Eq. (3) is proportional to the product of the defect cluster density and scattering cross-sectional area.

By effectively utilizing the regression curve obtained from the analysis presented in Fig. 4, the VDOP values, which could not be detected using the IR-T method, can be quantitatively determined from the XDS characteristic intensity. Figure 5 shows the relation with all data of measured XDS characteristic intensity and VDOP as well as the data obtained from TEM analysis. The black empty markers represent the data derived from both the XDS characteristic intensity and the IR-T measurement shown in Fig. 4, and the filled blue and orange markers represent the VDOP values derived from the XDS characteristic intensity by extrapolating the regression curves with the coefficients shown in Table III. The VDOP values less than or equal to 8×10^7 cm^{-3} (filled blue markers) for Samples A and B are plotted down to the value of 2×10^7 cm^{-3} cm which is lower than the value of 7×10^7 cm^{-3}, indicating that the XDS method can derive VDOP lower than the IR-T detection limit. In addition, for the VDOP values more than or equal to 5×10^9 cm^{-3} where the IR-T method cannot accurately detect due to overlapping scattering from OPs, the VDOP values can be derived from the XDS characteristic intensity (filled orange markers), which are plotted up to 1.1×10^{12} cm^{-3}. We observed OPs at a depth of 200 μm in Sample C by TEM, where the VDOP was above the detection limit of IR-T. An area of approximately 1.25×10^{-10} cm^3 was observed at 11,000 magnification, and a total of 55 OPs were found, which are also shown in Fig. 5. The plot measured by TEM matched well with the linear extrapolation up to a volume density of 5×10^9 cm^{-3} measured by IR-T. Thus, the XDS characteristic intensity can be used to quantitatively evaluate the VDOP over a wider range than IR-T.

In Table III, differences were observed between the intercept (a) and slopes (b) of the regression curves for Samples A–C. One of the factor is the morphology of OPs. According to Fujimori, OPs exhibit an octahedral shape when heat-treated at temperatures below 1000

°C and in an atmosphere with low oxygen supersaturation (as in Sample A), and a plate-like shape is dominant when heat-treated in an atmosphere with high oxygen supersaturation at temperatures below 1000 ℃ (as in Sample B and Sample C).[26] This is because OPs grow in a manner that minimizes the sum of the strain and interfacial energies, depending on the growth conditions.[27] According to Yonemura et al., the lattice distortion ($\Delta a/a$; a is the lattice constant) on silicon caused by plate-shaped OPs with side lengths of several hundred nanometers is very large distortion, which is about 3×10^{-3} near the flat plane and 1×10^{-3} near the edge of the plane. [28] Plate-like OPs grown under these conditions are highly distorted and may cause dislocation loops and punched-out dislocations.[29] In our samples, we observed such characteristics in the OPs. Figure 6 shows representative TEM images of OPs observed at a depth of 200 μm in Sample C. The OPs shown in Figs. 6 (a) and 6(b) are plate-like, whereas that in Fig. 6(c) is octahedral. The OPs in Fig. 6(a) were very large in size, exceeding 300 nm. The plate-like OPs accounted for 60% of the total, which was slightly lower than the values of 80–90% in CZ-Si wafers subjected to a typical heat treatment at 1000 °C with low oxygen supersaturation.[27] This is probably because, unlike the Ar heat treatment, RTO can leave a high concentration of residual vacancies in the bulk section;[20-22] thus, a certain number of octahedral-shaped OPs also exist.[30] Nevertheless, plate-like OPs held majority in the sample, and as shown in Figs. 6(a) and 6(b), they were accompanied by a strain field and dislocation loops. For Samples B and C, the average size measured by IR-T was less than 100 nm, but it is believed that the increased XDS intensity was due to the inclusion of plate-like OPs with sizes exceeding 100 nm. From the results and discussion above, the intercept of the extrapolation line (a) in Fig. 4 indicates the characteristic intensity reflecting the amount of strain in Si around the OPs with dislocations contained in the sample, both of which are larger than those for Sample A.

Sama et al.[14] and Bublik et al.[15] investigated the relation between XDS and OPs larger than 100 nm and observed dislocations and stacking faults in etched samples using an optical microscope. In contrast, our study revealed a strong relation between the XDS characteristic intensity and VDOP and AVOP, with an average size of less than 90 nm. In particular, the XDS analysis method used in this study is effective for the quantitative analysis of not only OPs accompanied by dislocations but also fine OPs without dislocations.

5. Conclusions

We investigated OPs in CZ-Si by analyzing the integrated intensity of XDS, including the Huang scattering, asymptotic scattering, and Stokes-Wilson scattering regions, obtained

from 2θ/ω scan of the surface of the obliquely polished CZ-Si wafers, with depth variation using a highly collimated synchrotron radiation X-ray diffractometer constructed at SPring-8. The XDS integrated intensity, especially in the region of Huang scattering, is closely related to the VDOP and AVOP derived from the IR-T observations. As a result, we found that X-rays scattered from depths below 40 μm contribute to the XDS characteristic intensity, which is critical for the quantitative analysis of OPs. The XDS characteristic intensity is an effective method for quantitatively analyzing minute OPs of 100 nm or less.

Acknowledgments

Synchrotron radiation experiments were performed at the BL24XU of SPring-8 with the approval of the Japan Synchrotron Radiation Research Institute (JASRI) (Proposal No. 2015B3265, 2016A3265, and 2017B3265). We thank Dr. Shingo Takeda of the SPring-8 Service and the students of the University of Hyogo for their cooperation in adjusting the diffractometer and conducting the experiments. This research was partly supported by JSPS KAKENHI Grants (JP22KK0055 and JP23H01447).

Conflict of Interest

The authors declare no conflict of interest.

References

1) A. Goda, MDPI Electron. **10** (24), 3156 (2021).
2) Y. Oike, M. Ikeda, A. Theuwissen, J. Solhusvik, J. Chang, and T. Kuroda, 2014 IEEE Int. Solid-State Circuit Conf. Dig. Tech. Papers (ISSCC), doi:10.1109/ISSCC.2014.6757541.
3) Y. Kagawa, and H. Iwamoto, *3DIC 2019*, (Japan, sendai, 2019) p. 1-4.
4) K. Hoshikawa, and X. Huang, Mater. Sci. Eng. B, **72**, (2000), p.73-79.
5) E. Orowan, Symposium on internal stresses in metals & alloys Institute of Metals (1948), p. 451.
6) D. Gilles, E. R. Weber, and S. Hahn, Phys. Rev. Lett., **64**, 196 (1990).
7) K. Sueoka, J. Electrochem. Soc., **152**(10), G731 (2005).
8) S. Maeda, H. Sudo, H. Okamura, K. Nakamura, Koji Sueoka, and Koji Izunome, J. Appl. Phys. **123**, 161591 (2018).
9) H. Sudo, K. Nakamura, S. Maeda, H. Okamura, K. Izunome, and K. Sueoka, ECS J. Solid State Sci. Technol. **8**, P35, (2019).
10) H. Sudo, K. Nakamura, H. Okamura, S. Maeda, and K. Sueoka, J. Appl. Phys. **131**, 055704 (2022).
11) K. Moriya, K. Hirai, K. Kashima, and S. Takasu, J. Phys., **66** (1989), p. 5267-5273.
12) H. Trinkaus, Phys. Stat. Sol. (b) **51**, 307 (1972).
13) P. H. Dederichs, J. Phys. F; Metal Phys. **3**, 471, (1973).
14) S. Sama, M. Porrini, F. Fogale, and M. Servidori, J. Electrochem. Soc., **148**(9) G517-G523, (2001).
15) V. T. Bublik, S. Y. Matsnev, K. D. Shcherbachev, M. V. Mezhennyi, M. G. Mil'vidskii, and V. Y. Reznik, Phys. Solid State, **45** (10), 2003, p. 1918-1925.
16) O. Caha, and M. Meduna, Physica B **404**, (2009), p. 4626-4629.
17) B. C. Larson, in : R. I. Barabash, G. E. Lee, and P. E. A. Turchi (Eds.), *Diffuse Scattering and the Fundamental Properties of Materials*, (Momentum Press, New York, 2009), p.139-160.
18) B. C. Larson, and W. Schmatz, Phys. Stat. Sol. (b), **99**, 267 (1980).
19) B. C. Larson, and F. W. Young JR., Phys. Stat. Sol., (a) **104**, 273 (1987).
20) K. Araki, S Maeda, T. Senda, H. Sudo, and H. Saito, ECS J. Solid State Sci. Technol. 2 P66, (2013).
21) K. Araki, S. Maeda, H. Sudo, T. Aoki, and K. Izunome, ECS Solid State Lett. **3** (9), P114, (2014).
22) K. Araki, H. Sudo, and S. Maeda, ECS Solid State Lett. **4** (9), P63, (2015).

23) K. Sueoka, N. Ikeda, T. Yamamoto, and S. Kobayashi, Jpn. J. Appl. Phys. **34**, 4599, (1995).
24) H. Takeno, Y. Hayamizu, and K Miki, J. Appl. Phys. **84**, 3113, (1998).
25) S. Takeda, K. Yokoyama, Y. Tsusaka, Y. Kagoshim, J. Matsuic, and A. Ogura, J. Synchrotron Rad. **13**, 2006, p. 373-377.
26) H. Fujimori, J. Electrochem. Soc. **144**, 3180, (1997).
27) W. A. Tiller, S. Hahn, and F. A. Ponce, J. Appl. Phys., **59**, 1986, p.3255.
28) M. Yonemura, K. Sueoka, and K. Kamei, Appl. Surf. Sci., 130-132, (1998), p.208-213.
29) K. Sueoka, M. Akatsuka, H. Katahama, and N. Adachi, J. Electrochem. Soc. **144**, 1111, (1998).
30) H. Sudo, Thesis, Okayama prefectural university, Okayama, Japan, (2021) [in Japanese].

Figure Captions

Fig. 1. Schematic of the test samples (Samples A–C). These samples were obliquely polished at 2.87°, and X-rays were irradiated on this polished surface from the [011] direction.

Fig. 2. XRCs near 400 diffraction for CZ-Si wafers (Samples A–C), where the vertical and horizontal axes represent normalized intensity and Qz converted from the diffraction angle, respectively, for (a) Sample A, (b) Sample B, and (c) Sample C.

Fig. 3. (a) Relation between XDS characteristic intensity and the volume density of oxygen precipitates measured by IR-T in Sample A. Depth range of the analysis area in the cross-sectional IR-T image was varied from 10 to 60 μm as illustrated in (b) where examples for the depth range 10 and 40 μm cases are shown.

Fig. 4. Relation diagram of the XDS characteristic intensity with (a) the volume density and (b) the average volume area of OPs in Samples A–C. For each sample, a 40 μm deep × 1000 μm wide area was selected to estimate the volume density and size of OPs from cross-sectional IR-T images.

Fig. 5. Relation diagram with all data of measured the XDS characteristic intensity and VDOP as well as those obtained from TEM analysis. The black empty markers represent the VDOP derived from the IR-T, and the filled blue and orange markers represent the VDOP derived from the XDS characteristic intensity by extrapolating the regression curves with coefficients shown in Table III. The asterisk marker indicates the data obtained by TEM at a depth of 200 μm in Sample C.

Fig. 6. Typical TEM images of OPs with (a) and (b) a plate-shape and (c) an octahedral-shape formed in Sample C. The OPs with (a) are ≥300 nm in size and have a strain field around this OPs. The OPs with (b) are surrounded by dislocations.

Table I. Heat treatment conditions of CZ-Si samples and resulting cross-sectional images measured by IR-T. The average size of OPs was calculated from IR-T images of OPs within the region contributing to XDS up to a depth of 40 μm, covering the area from the sample surface to a depth of 280 μm.

Samples	A	B	C	D (reference)
Wafer type	Cz-Si	Cz-Si	Cz-Si	Fz-Si
Heat treatment conditions	RTO + 1000°C/4 h (O_2) + 1000°C/4 h (Ar)	RTO + 780°C/4 h (O_2) + 1000°C/16h (O_2)	RTO + 1000°C/4 h (O_2) + 1000°C/4 h (Ar) + 780°C/4h (O_2) + 1000°C/16h (O_2)	Non
IR-T Images	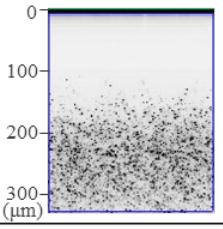	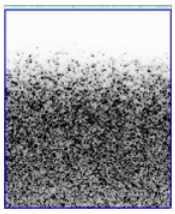	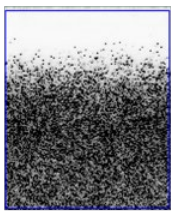	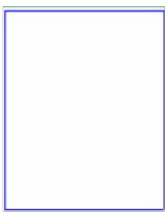
Size of OPs (nm)	47 ± 19	75 ± 25	82 ± 26	-

Table II. Conditions for $2\theta/\omega$ scan. Measurement steps, accumulation times, and attenuator conditions for each $2\theta/\omega$ scan range.

2θ scan range (deg.)	2θ scan steps (deg.)	Accumulation time (sec)	Attenuator
-0.36 ~ -0.16	1×10^{-2}	2.0	Non
-0.16 ~ -0.02	2×10^{-3}	1.5	Cu 30 μm
-0.02 ~ -0.004	4×10^{-4}	1.0	Cu 60 μm
-0.004 ~ -0.004	8×10^{-5}	1.0	Cu 120 μm
0.004 ~ 0.02	4×10^{-4}	1.0	Cu 60 μm
0.02 ~ 0.16	2×10^{-3}	1.5	Cu 30 μm
0.16 ~ 0.36	1×10^{-2}	2.0	Non

Table III. Coefficient values of the regression curve correlating the XDS characteristic intensity with the oxygen precipitate density and average cross-sectional area shown in Fig. 4.

	VDOP		AVOP	
	a	*b*	*a*	*b*
Sample A	5.12×10^{-7}	0.149	3.03×10^{-15}	2.75
Sample B	1.63×10^{-6}	0.216	3.65×10^{-13}	2.24
Sample C	3.85×10^{-6}	0.192	6.21×10^{-13}	2.22

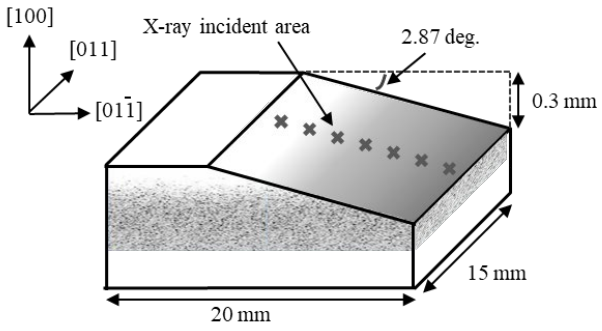

Fig. 1.

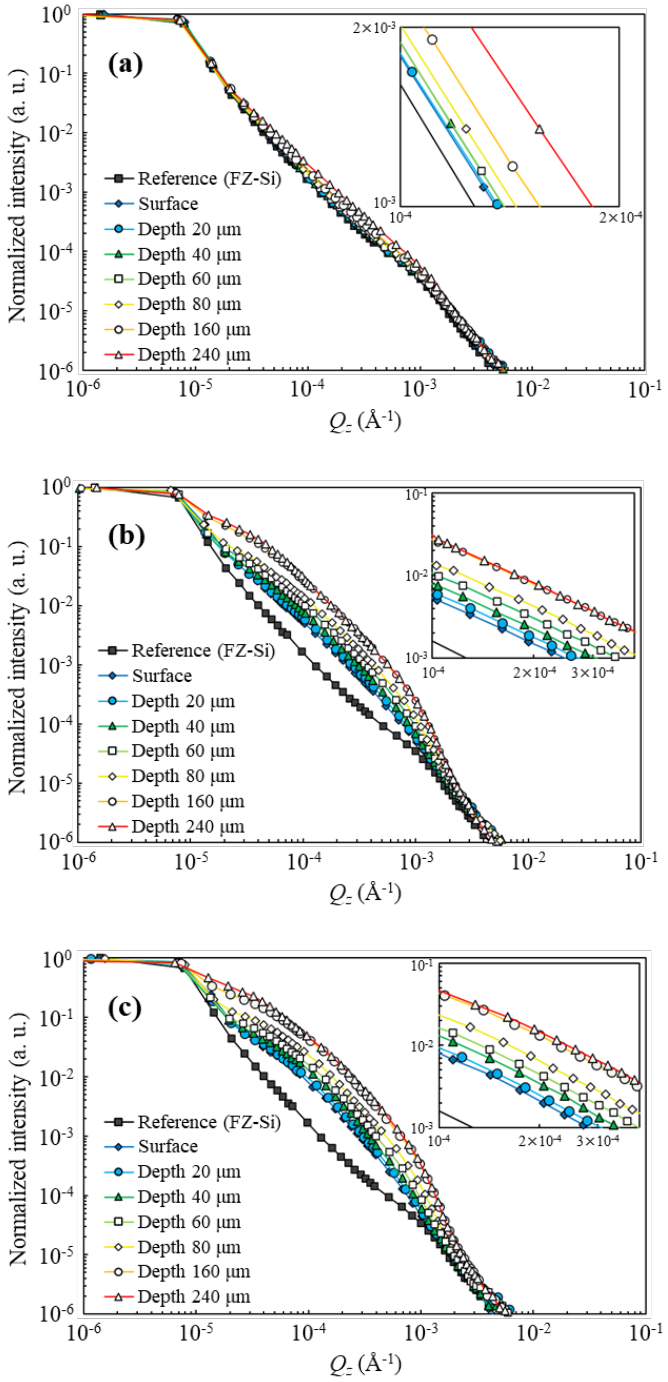
(a)
(b)
(c)
Normalized intensity (a. u.)
Q_z (Å^{-1})
Reference (FZ-Si)
Surface
Depth 20 μm
Depth 40 μm
Depth 60 μm
Depth 80 μm
Depth 160 μm
Depth 240 μm

Fig. 2.

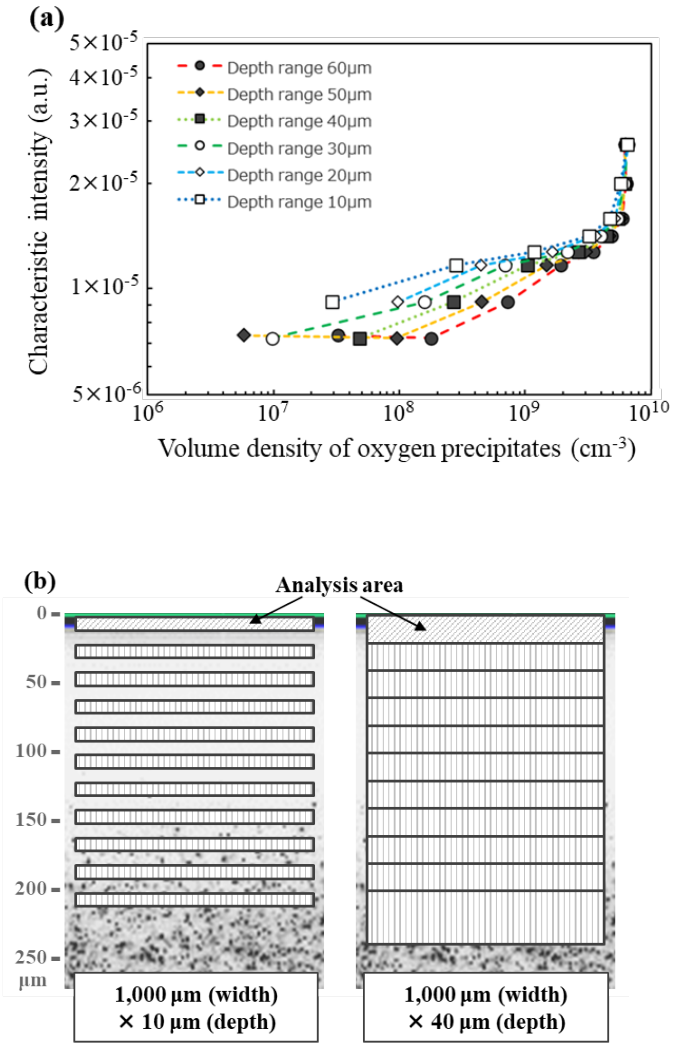
(a)
Characteristic intensity (a.u.)
5×10-5
4×10-5
3×10-5
2×10-5
1×10-5
5×10-6
Depth range 60μm
Depth range 50μm
Depth range 40μm
Depth range 30μm
Depth range 20μm
Depth range 10μm
10^6
10^7
10^8
10^9
10^10
Volume density of oxygen precipitates (cm-3)
(b)
Analysis area
0
50
100
150
200
250
μm
1,000 μm (width)
× 10 μm (depth)
1,000 μm (width)
× 40 μm (depth)

Fig. 3.

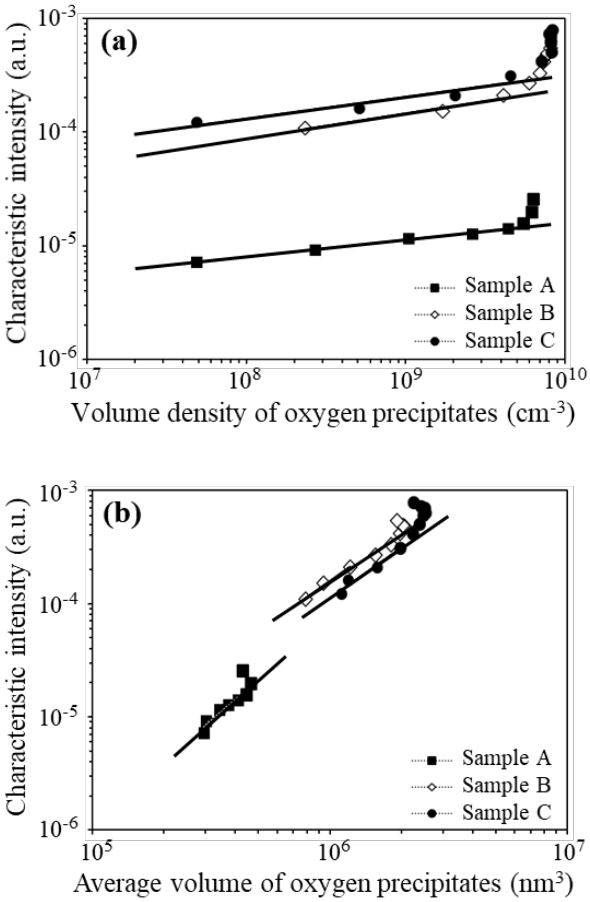
(a)
Characteristic intensity (a.u.)
Volume density of oxygen precipitates (cm-3)
Sample A
Sample B
Sample C
(b)
Characteristic intensity (a.u.)
Average volume of oxygen precipitates (nm3)
Sample A
Sample B
Sample C

Fig. 4.

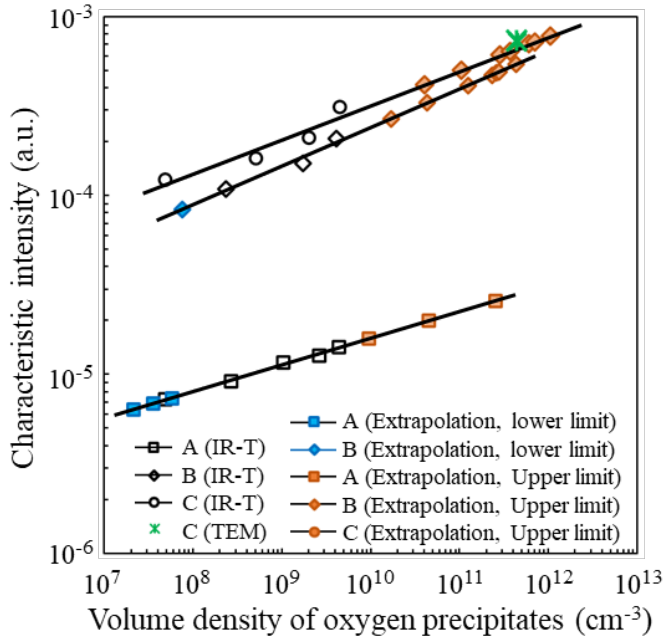
Characteristic intensity (a.u.)
10-3
10-4
10-5
10-6
107
108
109
1010
1011
1012
1013
Volume density of oxygen precipitates (cm-3)
A (IR-T)
B (IR-T)
C (IR-T)
C (TEM)
A (Extrapolation, lower limit)
B (Extrapolation, lower limit)
A (Extrapolation, Upper limit)
B (Extrapolation, Upper limit)
C (Extrapolation, Upper limit)

Fig. 5.

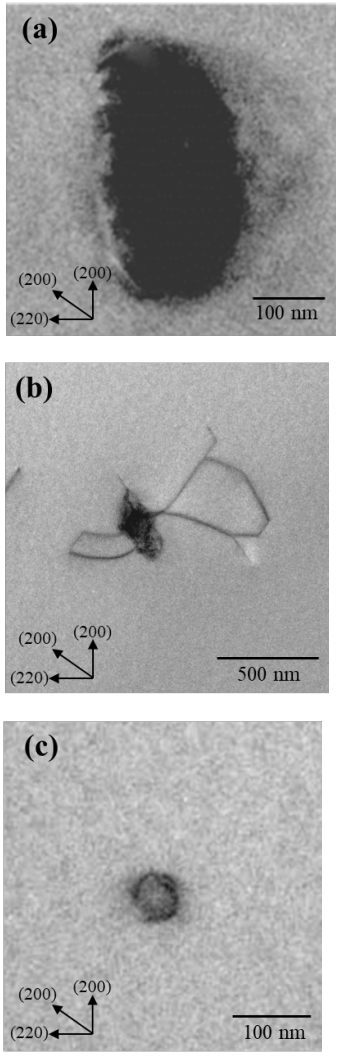

Fig. 6.